



Three-dimensional tomographic microscopy technique with multi-frequency combination with partially coherent illuminations

JIAJI LI,^{1,2,3} QIAN CHEN,^{1,2,4} JIASONG SUN,^{1,2,3} JIALIN ZHANG,^{1,2,3} JUNYI DING,^{1,2,3} AND CHAO ZUO^{1,2,3,*}

¹School of Electronic and Optical Engineering, Nanjing University of Science and Technology, No. 200 Xiaolingwei Street, Nanjing, Jiangsu Province 210094, China

²Jiangsu Key Laboratory of Spectral Imaging & Intelligent Sense, Nanjing University of Science and Technology, Nanjing, Jiangsu Province 210094, China

³Smart Computational Imaging Laboratory (SCILab), Nanjing University of Science and Technology, Nanjing, Jiangsu Province 210094, China

⁴chenqian@njust.edu.cn

*surpasszuo@163.com

Abstract: We demonstrate a three-dimensional (3D) optical diffraction tomographic technique with multi-frequency combination (MFC-ODT) for the 3D quantitative phase imaging of unlabeled specimens. Three sets of through-focus intensity images are captured under an annular aperture and two circular apertures with different coherence parameters. The 3D phase optical transfer functions (POTF) corresponding to different illumination apertures are combined to obtain a synthesized frequency response, achieving high-quality, low-noise 3D reconstructions with imaging resolution up to the incoherent diffraction limit. Besides, the expression of 3D POTF for arbitrary illumination pupils is derived and analyzed, and the 3D imaging performance of annular illumination is explored. It is shown that the phase-contrast washout effect in high-NA circular apertures can be effectively addressed by introducing a complementary annular aperture, which strongly boosts the phase contrast and improves the imaging resolution. By incorporating high-NA illumination as well as high-NA detection, MFC-ODT can achieve a theoretical transverse resolution up to 200 nm and an axial resolution of 645 nm. To test the feasibility of the proposed MFC-ODT technique, the 3D refractive index reconstruction results are based on a simulated 3D resolution target and experimental investigations of micro polystyrene bead and unstained biological samples are presented. Due to its capability for high-resolution 3D phase imaging as well as the compatibility with a widely available commercial microscope, the MFC-ODT is expected to find versatile applications in biological and biomedical research.

© 2018 Optical Society of America under the terms of the [OSA Open Access Publishing Agreement](#)

OCIS codes: (110.6960) Tomography; (100.5070) Phase retrieval; (100.3010) Image reconstruction techniques; (170.6900) Three-dimensional microscopy; (170.3880) Medical and biological imaging.

References and links

1. F. Zernike, "Phase contrast, a new method for the microscopic observation of transparent objects," *Physica* **9**(7), 686–698 (1942).
2. G. Nomarski and A. Weill, "Application à la métallographie des méthodes interférentielles à deux ondes polarisées," *Rev. Metall* **2**, 121–128 (1955).
3. M. K. Kim, *Digital Holographic Microscopy* (Springer, 2011).
4. P. Ferraro, D. Alferi, S. De Nicola, L. De Petrocellis, A. Finizio, and G. Pierattini, "Quantitative phase-contrast microscopy by a lateral shear approach to digital holographic image reconstruction," *Opt. Lett.* **31**, 1405–1407 (2006).
5. Z. Wang, L. Millet, M. Mir, H. Ding, S. Unarunotai, J. Rogers, M. U. Gillette, and G. Popescu, "Spatial light interference microscopy (SLIM)," *Opt. Express* **19**, 1016–1026 (2011).
6. B. Bhaduri, H. Pham, M. Mir, and G. Popescu, "Diffraction phase microscopy with white light," *Opt. Lett.* **37**, 1094–1096 (2012).

7. L. Waller, L. Tian, and G. Barbastathis, "Transport of intensity phase-amplitude imaging with higher order intensity derivatives," *Opt. Express* **18**, 12552–12561 (2010).
8. C. Zuo, Q. Chen, W. Qu, and A. Asundi, "High-speed transport-of-intensity phase microscopy with an electrically tunable lens," *Opt. Express* **21**, 24060–24075 (2013).
9. J. A. Rodrigo and T. Alieva, "Rapid quantitative phase imaging for partially coherent light microscopy," *Opt. Express* **22**, 13472–13483 (2014).
10. M. H. Jenkins, J. M. Long, and T. K. Gaylord, "Multifilter phase imaging with partially coherent light," *Appl. Opt.* **53**, D29–D39 (2014).
11. C. Zuo, J. Sun, J. Li, J. Zhang, A. Asundi, and Q. Chen, "High-resolution transport-of-intensity quantitative phase microscopy with annular illumination," *Sci. Rep.* **7**, 7654 (2017).
12. J. Li, Q. Chen, J. Zhang, Y. Zhang, L. Lu, and C. Zuo, "Efficient quantitative phase microscopy using programmable annular LED illumination," *Biomed. Opt. Express* **8**, 4687–4705 (2017).
13. L. Tian and L. Waller, "Quantitative differential phase contrast imaging in an LED array microscope," *Opt. Express* **23**, 11394–11403 (2015).
14. A. C. Kak and M. Slaney, *Principles of Computerized Tomographic Imaging* (SIAM, 2001).
15. E. Wolf, "Three-dimensional structure determination of semi-transparent objects from holographic data," *Opt. Commun.* **1**, 153–156 (1969).
16. V. Lauer, "New approach to optical diffraction tomography yielding a vector equation of diffraction tomography and a novel tomographic microscope," *J. Microsc.* **205**, 165–176 (2002).
17. W. Choi, C. Fang-Yen, K. Badizadegan, S. Oh, N. Lue, R. R. Dasari, and M. S. Feld, "Tomographic phase microscopy," *Nat. Methods* **4**, 717 (2007).
18. Y. Sung, W. Choi, C. Fang-Yen, K. Badizadegan, R. R. Dasari, and M. S. Feld, "Optical diffraction tomography for high resolution live cell imaging," *Opt. Express* **17**, 266–277 (2009).
19. Y. Cotte, F. Toy, P. Jourdain, N. Pavillon, D. Boss, P. Magistretti, P. Marquet, and C. Depeursinge, "Marker-free phase nanoscopy," *Nat. Photonics* **7**, 113 (2013).
20. K. Kim, J. Yoon, S. Shin, S. Lee, S.-A. Yang, and Y. Park, "Optical diffraction tomography techniques for the study of cell pathophysiology," *J. Biomed. Photon. Eng.* **2**, 10.18287/JBPE16.02.020201 (2016).
21. J. Yoon, K. Kim, H. Park, C. Choi, S. Jang, and Y. Park, "Label-free characterization of white blood cells by measuring 3D refractive index maps," *Biomed. Opt. Express* **6**, 3865–3875 (2015).
22. W. Krauze, A. Kuś, D. Śladowski, E. Skrzypek, and M. Kujawińska, "Reconstruction method for extended depth-of-field optical diffraction tomography," *Methods* **136**, 40–49 (2017).
23. A. Kuś, W. Krauze, and M. Kujawińska, "Limited-angle holographic tomography with optically controlled projection generation," *Proc. SPIE* **9330**, 933007 (2015).
24. S. Shin, K. Kim, J. Yoon, and Y. Park, "Active illumination using a digital micromirror device for quantitative phase imaging," *Opt. Lett.* **40**, 5407–5410 (2015).
25. K. Lee, K. Kim, G. Kim, S. Shin, and Y. Park, "Time-multiplexed structured illumination using a DMD for optical diffraction tomography," *Opt. Lett.* **42**, 999–1002 (2017).
26. C. Zuo, J. Sun, J. Zhang, Y. Hu, and Q. Chen, "Lensless phase microscopy and diffraction tomography with multi-angle and multi-wavelength illuminations using a LED matrix," *Opt. Express* **23**, 14314–14328 (2015).
27. R. Horstmeyer, J. Chung, X. Ou, G. Zheng, and C. Yang, "Diffraction tomography with Fourier ptychography," *Optica* **3**, 827–835 (2016).
28. J. Li, Q. Chen, J. Zhang, Z. Zhang, Y. Zhang, and C. Zuo, "Optical diffraction tomography microscopy with transport of intensity equation using a light-emitting diode array," *Opt. Laser Eng.* **95**, 26–34 (2017).
29. W. Gorski and W. Osten, "Tomographic imaging of photonic crystal fibers," *Opt. Lett.* **32**, 1977–1979 (2007).
30. Y. Jeon and C.-K. Hong, "Rotation error correction by numerical focus adjustment in tomographic phase microscopy," *Opt. Eng.* **48**, 105801 (2009).
31. A. Kuś, M. Dudek, B. Kemper, M. Kujawińska, and A. Vollmer, "Tomographic phase microscopy of living three-dimensional cell cultures," *J. Biomed. Opt.* **19**, 046009 (2014).
32. M. H. Jenkins and T. K. Gaylord, "Three-dimensional quantitative phase imaging via tomographic deconvolution phase microscopy," *Appl. Opt.* **54**, 9213–9227 (2015).
33. F. Merola, P. Memmolo, L. Miccio, R. Savoia, M. Mugnano, A. Fontana, G. D'ippolito, A. Sardo, A. Iolascon, A. Gambale, and P. Ferraro, "Tomographic flow cytometry by digital holography," *Light Sci. Appl.* **6**, e16241 (2017).
34. M. M. Villone, P. Memmolo, F. Merola, M. Mugnano, L. Miccio, P. L. Maffettone, and P. Ferraro, "Full-angle tomographic phase microscopy of flowing quasi-spherical cells," *Lab Chip* **18**, 126–131 (2018).
35. N. Streibl, "Three-dimensional imaging by a microscope," *J. Opt. Soc. Am. A* **2**, 121–127 (1985).
36. M. Chen, L. Tian, and L. Waller, "3D differential phase contrast microscopy," *Biomed. Opt. Express* **7**, 3940–3950 (2016).
37. Y. Bao and T. K. Gaylord, "Quantitative phase imaging method based on an analytical nonparaxial partially coherent phase optical transfer function," *J. Opt. Soc. Am. A* **33**, 2125–2136 (2016).
38. J. M. Soto, J. A. Rodrigo, and T. Alieva, "Label-free quantitative 3D tomographic imaging for partially coherent light microscopy," *Opt. Express* **25**, 15699–15712 (2017).
39. J. M. Soto, J. A. Rodrigo, and T. Alieva, "Optical diffraction tomography with fully and partially coherent illumination in high numerical aperture label-free microscopy," *Appl. Opt.* **57**, A205–A214 (2018).

40. J. A. Rodrigo, J. M. Soto, and T. Alieva, "Fast label-free microscopy technique for 3D dynamic quantitative imaging of living cells," *Biomed. Opt. Express* **8**, 5507–5517 (2017).
41. T. Noda, S. Kawata, and S. Minami, "Three-dimensional phase contrast imaging by an annular illumination microscope," *Appl. Opt.* **29**, 3810–3815 (1990).
42. C. Zuo, Q. Chen, Y. Yu, and A. Asundi, "Transport-of-intensity phase imaging using Savitzky-Golay differentiation filter-theory and applications," *Opt. Express* **21**, 5346–5362 (2013).
43. M. H. Jenkins and T. K. Gaylord, "Quantitative phase microscopy via optimized inversion of the phase optical transfer function," *Appl. Opt.* **54**, 8566–8579 (2015).
44. J. Lim, K. Lee, K. H. Jin, S. Shin, S. Lee, Y. Park, and J. C. Ye, "Comparative study of iterative reconstruction algorithms for missing cone problems in optical diffraction tomography," *Opt. Express* **23**, 16933–16948 (2015).
45. Y. Sung, W. Choi, N. Lue, R. R. Dasari, and Z. Yaqoob, "Stain-free quantification of chromosomes in live cells using regularized tomographic phase microscopy," *PLoS ONE* **7**, e49502 (2012).

1. Introduction

The refractive index (RI) of biological cells and tissues contain important biophysical information about shapes, sizes, volumes and dry mass, and these characteristics are crucial for the morphological detection and diagnosis of disease. There are several qualitative and quantitative methods which have been proposed to provide reliable rendering about phase contrast and quantitative phase change introduced by the heterogeneous RI distribution within the label-free samples. Zernike phase contrast (PhC) microscopy [1] and differential interference contrast (DIC) microscopy [2] can effectively visualize the transparent biological samples by converting the phase into intensity, which have been widely used in cell biology studies. Alternatively, quantitative phase imaging (QPI) microscopy provides the quantitative data interpretation and phase reconstruction, and this imaging technique can be realized by the interferometric and non-interferometric approaches. The conventional off-axis digital holographic microscopy (DHM) [3, 4] has been developed to measure the total phase delay quantitatively, and some other interferometric methods based on common path geometries have been also proposed to improve the imaging quality and spatial resolution of the phase measurement by using spatial light modulator (SLM) or white-light sources [5, 6]. In addition, there are also numerous variants of non-interferometric phase retrieval approaches, like transport of intensity equation (TIE) [7–12] and differential phase contrast (DPC) [13], which provide promising QPI results under both coherent illumination and partially coherent illumination.

When the thickness of object is larger than the depth of field (DOF) of microscope, a single two-dimensional (2D) integral phase image is insufficient for the characterization of heterogeneous object, and the detailed volumetric information inside the sample is inaccessible. Three-dimensional (3D) RI distribution indeed enables the intracellular observation of biological samples, which can be recovered based on different tomographic approaches. The off-axis and common-path holographic microscopes are applied to the implementation of 3D label-free RI imaging with computerized tomography or optical diffraction tomography (ODT) based on the Fourier diffraction theorem [14–16]. In coherent ODT (C-ODT), the incident angle of coherent beam is changed by the rotating mirror [17–22], liquid crystal SLM [23], digital micro-mirror device (DMD) [24, 25] or light-emitting diode (LED) array [26–28]. The maximum coverage of illumination angle is determined by the NA of the condenser lens, and the incomplete range of incident angle leads to a missing cone problem due to the finite NA. Alternatively, in sample rotation ODT, the mechanical rotation of the object enables a more complete angular coverage, but the radial run-out of rotation inevitably makes the sample unstable [20, 29]. Although the reconstruction artifacts of object rotation can be minimized by some numerical methods [30, 31], this type of C-ODT is more suitable for certain solid non-biological objects than biological samples [29, 32]. Instead of using a complex setup for rotating or illuminating the sample from several directions, the random self-rotation of cells in microfluidic flow has recently been exploited to achieve full-angle ODT, which allows fast single-cell analysis in high-throughput continuous-flow cytotomography and simplifies the optical system significantly [33, 34].

On a different note, ODT can also be implemented based on a conventional bright-field microscope with partially coherent illumination [35]. In partially coherent ODT (PC-ODT), the 3D RI distribution can be directly recovered from a through-focus intensity stack by using the inversion of 3D phase optical transfer function (POTF) of the imaging system. For a condenser aperture with a determined NA, the spatial frequency components of the object scattering potential transmitted by the PC-ODT are the same as the C-ODT under various angles of illumination within the maximum NA. Thus, the PC-ODT is very suitable for 3D QPI based on a traditional bright-field microscope. Many interesting diffraction tomographic approaches under partially coherent illumination have been developed very recently. M. Chen *et al.* [36] extended the 2D DPC quantitative imaging into 3D RI measurement by introducing an additional axial scanning process. The 3D RI reconstruction is achieved by a 3D fast Fourier transform (FFT) based deconvolution, without an intermediate 2D phase retrieval step. Y. Bao and T. Gaylord [37] extended Streibl's OTF theory and derived the analytical expression of 3D POTF for the non-paraxial case. Besides, J. Soto *et al.* [38,39] and J. Rodrigo *et al.* [40] adopted the non-paraxial POTF model for 3D phase deconvolution and obtained excellent 3D RI reconstruction results of biological samples recently. However, as pointed in [38], the phase contrast progressively vanishes as the illumination NA approaches the objective NA, suggesting that the phase information can hardly be transferred into intensity when the illumination NA is large. In the case of partially coherent illumination, the maximum achievable lateral resolution is determined by the sum of the objective NA and the illumination NA, where the ratio of illumination NA to objective NA (NA_{ill}/NA_{obj}) is so-called coherence parameter [35,38]. In other words, the intensity image gives no phase contrast under incoherent illumination when the coherence parameter equals 1 ($NA_{ill} = NA_{obj}$). Despite the doubled lateral resolution, the amplitude of the 3D POTF is significantly attenuated and the signal-to-noise ratio (SNR) of intensity stack is too poor to recover the 3D phase distribution. So, there is an inherent tradeoff between phase contrast and imaging resolution in the PC-ODT, which prevents the maximum possible resolution ($2NA_{obj}$) for 3D phase imaging. Note that the similar phenomenon has previously been observed in defocus-based 2D QPI techniques like the TIE [9, 10].

In this work, we demonstrate a 3D ODT technique with multi-frequency combination (MFC-ODT) for the RI measurement of unlabeled specimen based on a commercial inverted microscope. Three through-focus intensity stacks are captured under three illumination apertures including an annular aperture and two circular apertures with different coherent parameters. The optimal frequency components of 3D POTF corresponding to multiple illumination apertures are combined together by utilizing linear least-squares method, and a more accurate 3D reconstruction result with imaging resolution up to the incoherent diffraction limit can be obtained. By incorporating high-NA illumination as well as high-NA detection, MFC-ODT can achieve a theoretical transverse resolution up to 200 nm and an axial resolution of 645 nm, as predicted by the simulations. Although many previous works have provided complete theories about 3D POTF for PC-ODT [35,37] and demonstrated promising 3D RI experimental results [38–40] based on circular illumination aperture, the tradeoff between the intensity contrast and the maximum theoretical resolution has not been overcome yet in PC-ODT. The novelty of this work is to propose a tomographic technique with MFC by invoking different illumination apertures (especially the annular aperture) to synthesize an optimized frequency response. The annular aperture enhances the amplitude of the POTF on the Ewald sphere for both low and high frequencies in Fourier space. Not only the theoretical lateral resolution can be extended to twice the coherent diffraction limit, but also strong intensity contrast is retained even when the maximum NA of illumination optics is utilized.

The remainder of this paper is organized as follows. In Section 2, the numerical expression of 3D OTF for arbitrary illumination source is firstly re-derived based on the previous work, especially for annular illumination aperture. Next, comprehensible simulations are presented

for the characterization of 3D POTFs corresponding to different illumination aperture. Then the MFC-ODT method is introduced, and an intuitive explanation about optimized frequency coverage of the used aperture setting are provided. The experimental setup, data acquisition and reconstruction process are presented in Section 3. Section 4 shows the experimental analysis and investigations of micro polystyrene bead for different illumination apertures, and the 3D reconstruction results of unstained biological samples are presented as well. The work ends with discussion and concluding remarks.

2. Principle

2.1. Numerical expression of 3D POTF for arbitrary illumination aperture

The main purpose of ODT is to reconstruct the 3D RI distribution of the specimen, but this information is included in the optical scattering potential of heterogeneous medium. The scattering potential [15, 35] of object is defined by the function $V(\mathbf{r}) = k_0^2 [n^2(\mathbf{r}) - n_m^2]$, where k_0 is the wave number $2\pi/\lambda_0$ with λ_0 being the wavelength in free-space, $n(\mathbf{r})$ and n_m are the RI of specimen and its surrounding medium, correspondingly. The complex RI $n(\mathbf{r})$, which equals $n_p(\mathbf{r}) + i \cdot n_a(\mathbf{r})$, contains the sample's RI n_p and the absorptivity n_a . While the sample only modulates the phase of transmitted field, the complex RI and scattering potential function are always real.

In bright-field transmission microscope, N. Streibl [35] and Y. Bao *et al.* [37] presented the analytical form of 3D OTF for partially coherent illumination with circular aperture in the paraxial and non-paraxial regime, respectively. Before the derivation of 3D OTF formula for arbitrary illumination aperture, let us review some previous works about the 3D image formation in partially coherent microscope. 3D image formation under partially coherent illumination can be described as a 3D convolution between the object and point spread function (PSF) of system by invoking the Born approximation (weak scattering object) [35]. The measured intensity image stack is expressed as a linear superposition of the real and imaginary parts of the object scattering potential convolved with the corresponding PSFs $H_P(\mathbf{r})$ and $H_A(\mathbf{r})$:

$$I(\mathbf{r}) = B + \Phi(\mathbf{r}) \otimes H_P(\mathbf{r}) + A(\mathbf{r}) \otimes H_A(\mathbf{r}) \quad (1)$$

where B is the background intensity and can be understood as the un-scattered light or transmitted light, $\Phi(\mathbf{r})$ and $A(\mathbf{r})$ are the respective real and imaginary parts of object scattering potential function. Implementing the 3D FFT to above Eq. (1), the 3D spectrum of intensity stack is given by the sum of delta function and the product of scattering potential spectrum with corresponding transfer function in Fourier space:

$$\tilde{I}(\zeta) = B\delta(\zeta) + \tilde{\Phi}(\zeta)T_P(\zeta) + \tilde{A}(\zeta)T_A(\zeta) \quad (2)$$

where $\tilde{\Phi}(\zeta)$, $\tilde{A}(\zeta)$, T_P and T_A are the 3D phase spectrum, absorption spectrum, POTF and amplitude optical transfer function (AOTF), respectively. Here, we skip the complicated derivation of 3D OTF in [35] and directly give the generally 3D POTF of microscope in non-paraxial regime [37, 41]:

$$T_P(\rho, w) = \frac{j\lambda}{4\pi} \iint P\left(\rho' + \frac{1}{2}\rho\right) P^*\left(\rho' - \frac{1}{2}\rho\right) \left[S\left(\rho' + \frac{1}{2}\rho\right) - S\left(\rho' - \frac{1}{2}\rho\right) \right] \delta\left[w + \sqrt{\lambda^{-2} - \left(\rho' - \frac{1}{2}\rho\right)^2} - \sqrt{\lambda^{-2} - \left(\rho' + \frac{1}{2}\rho\right)^2} \right] d^2\rho' \quad (3)$$

where $\zeta = (\rho, w)$, P and P^* are the conjugated pair of aperture functions for a circular objective pupil, and S is the intensity distribution of illumination source. The definition of objective pupil

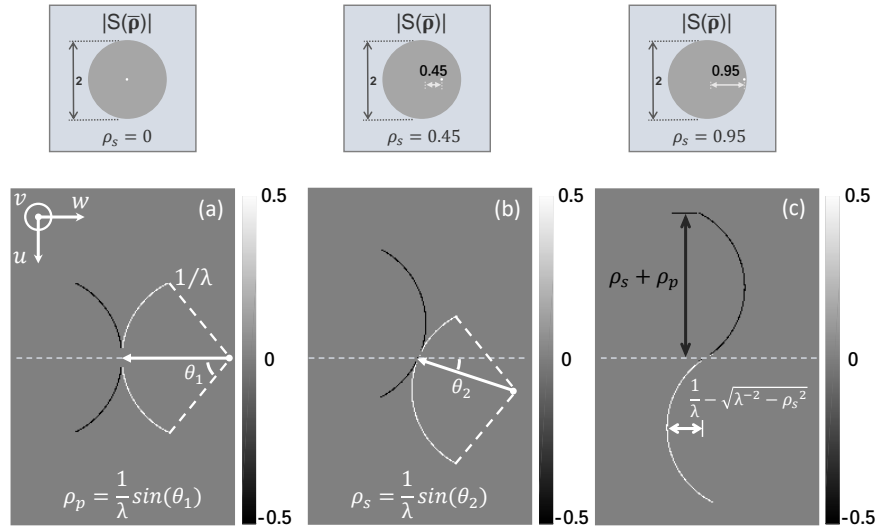


Fig. 1. 2D sections of 3D POTF for oblique coherent source with different normalized illumination NA. The radius of Ewald sphere is $1/\lambda$, and the normalized objective NA ρ_p and illumination NA ρ_s are $\sin(\theta_1)/\lambda$ and $\sin(\theta_2)/\lambda$, respectively. The lateral and axial resolution limits are $\rho_s + \rho_p$ and $1/\lambda - \sqrt{\lambda^{-2} - \rho_s^2}$, respectively.

function can be expressed as:

$$P(\rho) = \begin{cases} 1, & \text{if } |\rho| \leq \rho_p \\ 0, & \text{if } |\rho| > \rho_p \end{cases} \quad (4)$$

where ρ_p represents the normalized frequency (equals 1) corresponding to the objective NA. For the most common circular light source, the intensity of illumination is uniformly distributed over the illumination aperture, which can be represented as:

$$S(\rho) = \begin{cases} 1, & \text{if } |\rho| \leq \rho_s \\ 0, & \text{if } |\rho| > \rho_s \end{cases} \quad (5)$$

where ρ_s denotes the normalized frequency corresponding to the illumination NA. In this case, the POTF can be represented analytically, and the complete form of 3D POTF can be found in the appendix of [37] and [38].

Considering an arbitrary coherent source located on the source plane as shown in Fig. 1, and the distance from this point source to the center of pupil is ρ_s , represented as follows:

$$S(u, v) = \delta(u - \rho_s, v) \quad (6)$$

Substituting this source pupil function Eq. (6) into Eq. (3) results in a 3D POTF for oblique coherent illumination, and the analytical expression can be greatly simplified as:

$$T_p(u, v, w) = \frac{j\lambda}{4\pi} P^*(\rho_s - u, -v) \delta \left[w - \sqrt{\lambda^{-2} - \rho_s^2} + \sqrt{\lambda^{-2} - (\rho_s - u)^2 - v^2} \right] - \frac{j\lambda}{4\pi} P(\rho_s + u, v) \delta \left[w + \sqrt{\lambda^{-2} + \rho_s^2} - \sqrt{\lambda^{-2} - (\rho_s + u)^2 - v^2} \right] \quad (7)$$

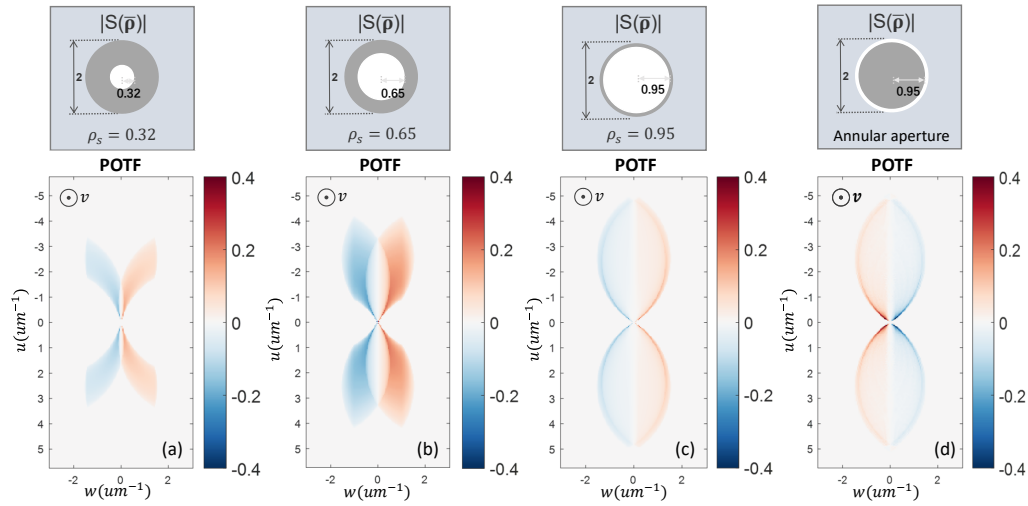


Fig. 2. 2D plots of 3D POTF section in $u - w$ plane for four different illumination apertures including circular and annular illumination apertures with different coherence parameters.

where $P^*(\rho_s - u, -v)$ and $P(\rho_s + u, v)$ are two conjugated aperture functions shifted by the oblique coherent source in 3D Fourier space, and these two delta functions are two shifted Ewald spheres defined by functions $(w + \sqrt{\lambda^{-2} + \rho_s^2})^2 + (\rho_s + u)^2 + v^2 = \lambda^{-2}$ and $(w - \sqrt{\lambda^{-2} - \rho_s^2})^2 + (\rho_s - u)^2 + v^2 = \lambda^{-2}$, respectively. Figure 1 shows the 2D section plots of 3D POTF for three different coherent sources, and these curves are consistent with the previous results [15, 16, 37–39]. The arc of Ewald sphere is shifted by incident light $S(u, v)$ and limited by the shifted objective pupil functions $P(u, v)$ in 2D sections. Besides, the amplitude of POTF is normalized by zero frequency component of AOTF, and the achievable lateral and axial resolution of 3D POTF is extended to the maximum value when ρ_s is equal to ρ_p .

For an illumination aperture of arbitrary shape, the illumination pattern can be discretized into a lot of coherent point sources with finite size, including both on-axis and oblique ones. The expression of circular illumination pupil can be written as the sum of delta function in Eq. (5). Moreover, the expression for annular illumination aperture can be defined as follows:

$$S(\rho) = \sum_{i=1}^N \delta(\rho - \rho_i), \quad |\rho_i| \approx \rho_p \quad (8)$$

where N is the number of discrete light points which satisfy this expression on the source plane. Substituting the pupil function Eq. (5) or Eq. (8) into Eq. (3) results in 3D POTF for circular or annular illumination aperture.

The plots of 3D POTF sections in $u - w$ plane for four different illumination apertures are illustrated in Fig. 2. The coherence parameter ρ_s in Figs. 2(a)-2(c) ranges from 0.32 to 0.95 for circular apertures, and the inner radius of annular aperture is 0.95 in Fig. 2(d). The lateral and axial resolutions are enhanced with the increase of coherence parameter, while the amplitude of POTF is attenuated, as demonstrated in Figs. 2(a)-2(c). These results are coincident with the well-known phenomenon that opening up condenser aperture of a microscope tends to reduce the contrast for phase information. Nevertheless, the POTF of annular aperture not only provides the extension of twice lateral resolution of coherent diffraction limit, but also improves the low frequency component of POTF around zero frequency point. Thus, the 3D OTFs (including POTF and AOTF) can be derived using numerical expression Eq. (5) and Eq. (8) for an arbitrary

illumination aperture, especially for circular and annular illumination apertures. Besides, if the asymmetric aperture is discretized into the superposition of coherent source like Eq. (8), the 3D OTF of DPC [36] can be calculated using the principle above as well.

2.2. Characterization of 3D POTF for partially coherent illumination

In this subsection, we simulate a microscopic system with different circular and annular illumination apertures, and analyze the effect of 3D POTF on the resolution and SNR of RI reconstruction. In the first row of Fig. 3, we show the sections of corresponding PSFs under circular apertures with $\rho_s = 0.65$, $\rho_s = 0.95$ and annular aperture with same parameter 0.95. The selected half subregions of each PSF section are enlarged in the corresponding subset to illustrate the intensity distribution more clearly. As can be seen, the intensity contrast of PSFs of circular source with $\rho_s = 0.65$ and annular one are much higher than the PSF contrast of circular source with coherent parameter 0.95. And the diffraction patterns of annular aperture are easier to distinguish. To further demonstrate how the illumination aperture affect the image contrast, we simulate an ideal phase micro bead (bead diameter $D_{bead} = 2 \mu\text{m}$, bead RI $n_{bead} = 1.59$, medium RI $n_m = 1.58$), which is convolved with the corresponding PSF to obtain the through-focus intensity stack, as illustrated in the second row of Fig. 3. The diffraction angle of defocused intensity images are same as the maximum illumination angle for each aperture with coherence parameter ρ_s . But the contrast of intensity image of bead under annular source is opposite to that of the traditional circular aperture, which is consistent with the distribution of OTF and PSF

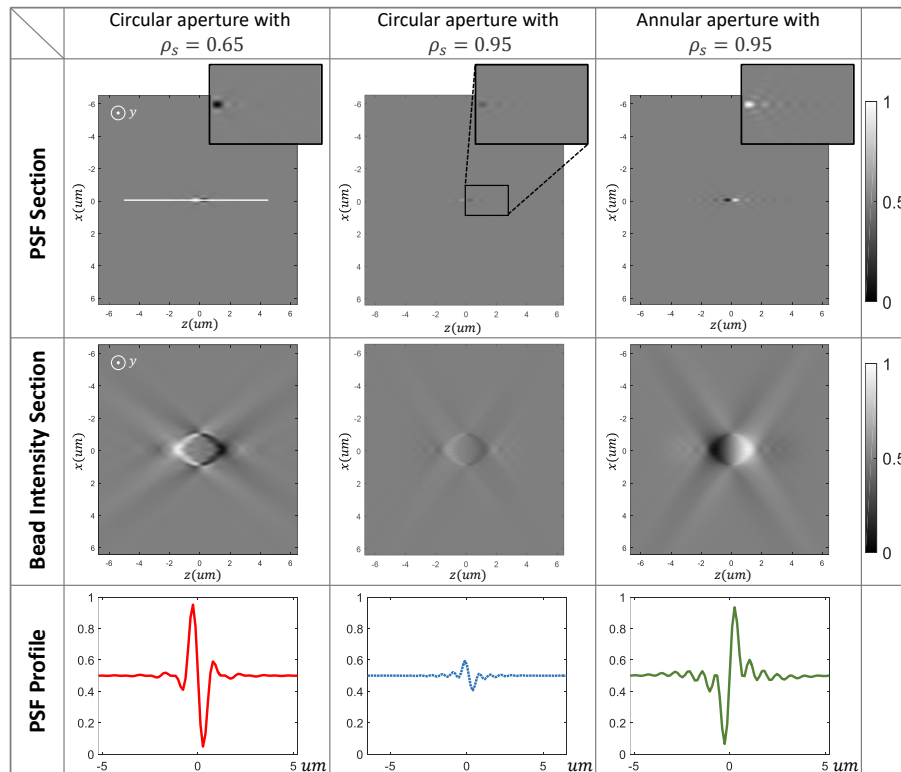


Fig. 3. The analysis of PSF for circular apertures with different coherence parameters and annular aperture. The intensity section of an ideal phase micro bead convolved different PSFs and the profiles of PSFs are plotted as well.

of annular illumination source. The average of these intensity images are normalized to 0.5. In addition, the profiles of PSFs are plotted in the last row of Fig. 3 to give more intuitive results about the characteristics of each illumination aperture. From these results, it can be concluded that the annular aperture not only provides strong intensity contrast but also retains the high frequency component among these illumination apertures.

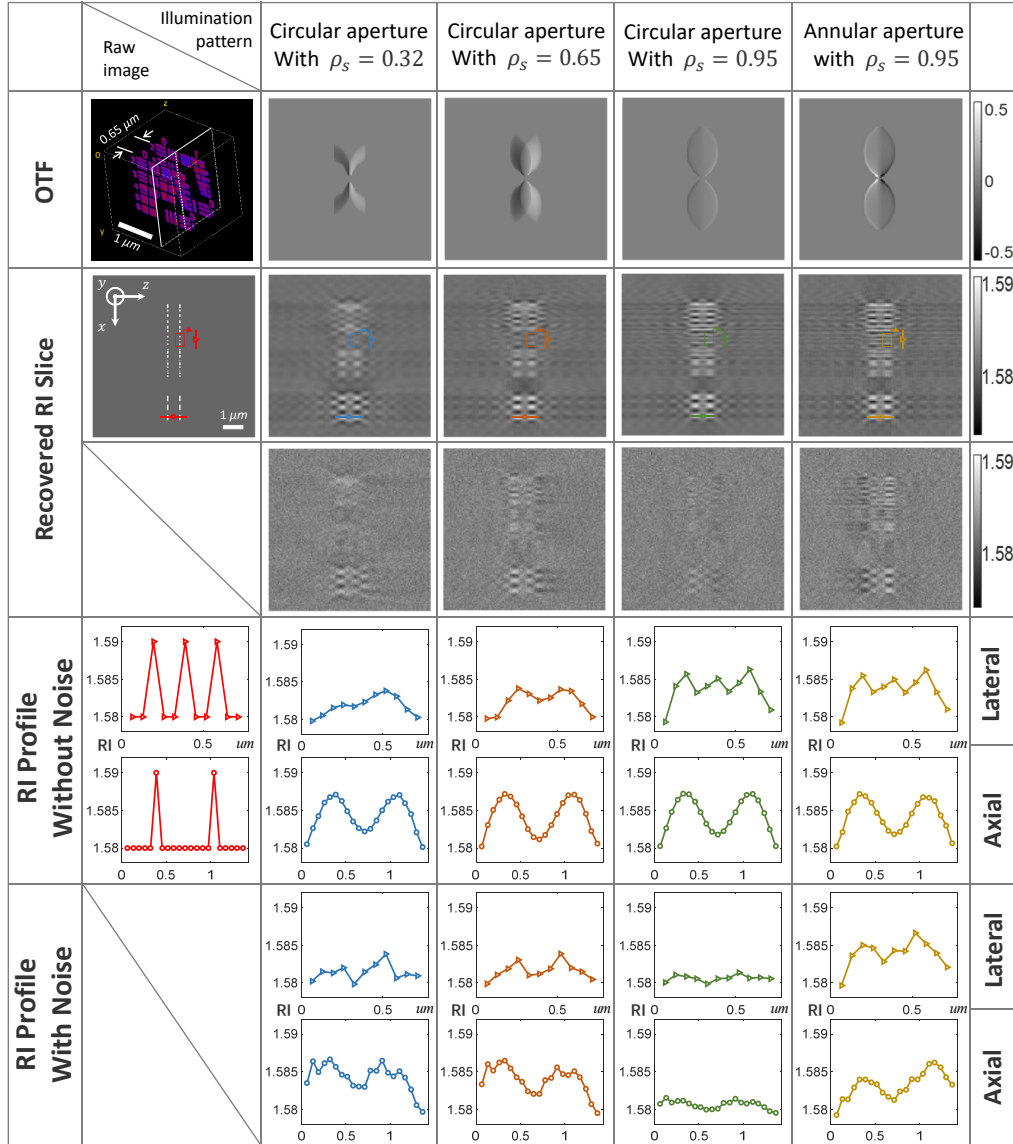


Fig. 4. 3D RI reconstruction results of a simulated 3D phase resolution target under noise-free situation and the Gaussian noise with a standard deviation of 0.15. The 3D phase object is composed of two same resolution target images placed in the different axial planes, and the distance between two resolution targets is $0.65 \mu\text{m}$ in the axial direction. The dimensions of this 3D object are $128 \times 128 \times 128$ pixels with the spatial sample rate $0.065 \mu\text{m}$ in both x , y and z directions. The RI of resolution target n is 1.59 with the surrounding medium RI $n_m = 1.58$. Scale bar, $1 \mu\text{m}$.

Next, we quantitatively analyze the effect of 3D POTF on the resolution and SNR of RI reconstruction for various illumination apertures. And the direct deconvolution formula (Eq. (4) in [38]) are utilized for the 3D RI reconstruction of a simulated 3D phase resolution target. Two identical 2D resolution targets are placed in the different axial planes to form a 3D phase object, and the RI contrast between resolution target and surrounding medium is 0.01 with the surrounding medium RI $n_m = 1.58$. Note that the system parameters ($NA_{ill} = NA_{obj} = 1.4$, central wavelength $\lambda_0 = 550$ nm) are the same with actual one in experimental setup in Section 3 except that the intensity stack contains only $128 \times 128 \times 128$ pixels. The lateral and axial sampling rates are both $0.065 \mu\text{m}$. The maximum theoretical lateral resolution $\lambda_0/(NA_{ill} + NA_{obj})$ is about $0.2 \mu\text{m}$, thus the resolution target elements with line pitch of $0.195 \mu\text{m}$ are chosen as the observed object to be recovered in the lateral direction. As for the axial resolution, the maximum resolution $\lambda_0/(n_m - \sqrt{n_m^2 - NA_{ill}^2})$ is about $0.645 \mu\text{m}$, so the distance between two layers of resolution target is set to $0.65 \mu\text{m}$ (10 pixels) in the axial direction.

Figure 4 show the reconstruction results of the 3D phase resolution target, and the first column of Fig. 4 are the raw RI slice and RI profiles without noise. It can be seen that the three-bar element can only be resolved by using the circular and annular apertures with the same coherence parameter 0.95 under noise-free condition. However, the axial RI profiles do not change too much for these four different illumination apertures because the lateral resolution improves faster than the axial resolution with the increase of objective NA and illumination NA. In order to characterize the noise sensitivity of different POTFs, Gaussian noise with a standard deviation of 0.15 is added to intensity images. The recovered results are shown in the last two rows of Fig. 4, and the lateral RI profile is only discernible under annular illumination aperture. For circular aperture with $\rho_s = 0.95$, the RI curves of resolution target elements are almost impossible to recover from the intensity image stack due to the poor SNR of its POTF. Though the maximum recovered frequency is determined by the sum of objective NA and illumination NA, the circular shape source cannot provide enough image contrast when the illumination NA approaches the objective NA. In contrast, the annular illumination aperture can effectively extend the lateral resolution to twice NA of objective while maintain a high level of the intensity contrast.

2.3. Multi-frequency combination of 3D POTFs

The 3D POTF of annular aperture can provide strong responses in both low and high frequencies on the Ewald sphere, but the response of intermediate frequency in the entire volume transmitted through the incoherent system is not sufficient. So in order to obtain a more complete frequency coverage and balanced transfer function, we propose a multi-frequency combination scheme that incorporates three intensity stacks to obtain a synthesized 3D POTF, resulting in high-quality 3D RI reconstruction with improved resolution and SNR. The three intensity stacks are captured under three illumination apertures with different shapes and coherent parameters, and the optimal frequency components of determined respective 3D POTF are combined together. Figure 5 illustrates a flow chart of MFC method. Three captured intensity sets are transferred into 3D Fourier space, and the 3D Fourier spectrum is deconvoluted by their corresponding POTF to obtain an estimated 3D scattering potential spectrum. Then, the 3D scattering potential spectrum sets are weighted according to different weighting parameters, and the final 3D scattering potential distribution is recovered by implementing an inverse 3D FFT. This process can be summarized as follows:

$$\Phi(\mathbf{r}) = \mathcal{F}^{-1} \left[\frac{\tilde{I}_1(\boldsymbol{\zeta})}{T_{P1}(\boldsymbol{\zeta})} \varepsilon_1 + \frac{\tilde{I}_2(\boldsymbol{\zeta})}{T_{P2}(\boldsymbol{\zeta})} \varepsilon_2 + \frac{\tilde{I}_3(\boldsymbol{\zeta})}{T_{P3}(\boldsymbol{\zeta})} \varepsilon_3 \right] \quad (9)$$

where \mathcal{F}^{-1} denotes the inverse 3D FFT. $\tilde{I}(\boldsymbol{\zeta})$ and $T_P(\boldsymbol{\zeta})$ are the 3D intensity Fourier spectrum and POTF of a certain aperture, respectively. And ε is the weighting parameter for each Fourier

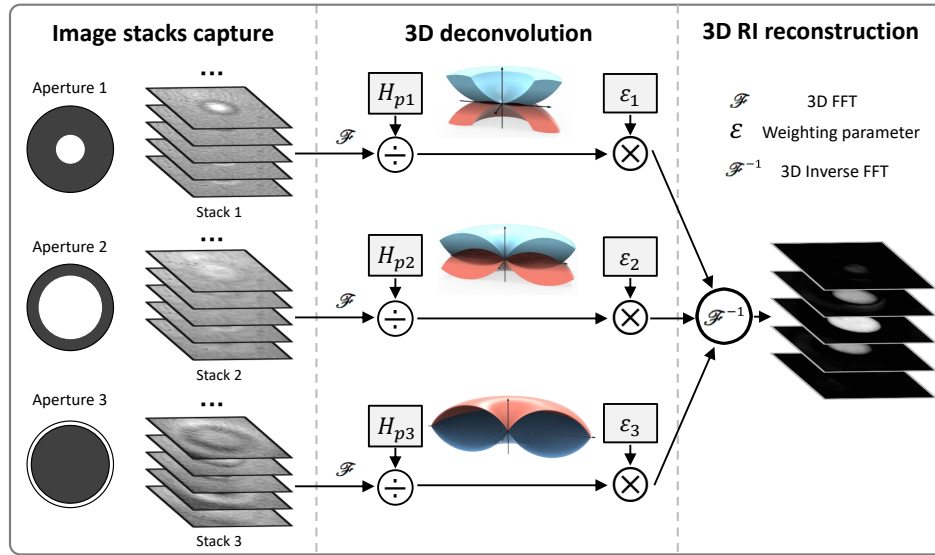


Fig. 5. Block diagram representation of the MFC-ODT method.

spectrum and is calculated by linear least-squares method among three sets of POTF:

$$\varepsilon_i = \frac{T_{P_i}^*(\zeta) T_{P_i}(\zeta)}{|T_{P_1}(\zeta)|^2 + |T_{P_2}(\zeta)|^2 + |T_{P_3}(\zeta)|^2}. \quad (10)$$

Substituting Eq. (10) into Eq. (9) results the final expression of 3D RI reconstruction:

$$\Phi(\mathbf{r}) = \mathcal{F}^{-1} \left[\frac{\tilde{I}_1(\zeta) T_{P_1}^*(\zeta) + \tilde{I}_2(\zeta) T_{P_2}^*(\zeta) + \tilde{I}_3(\zeta) T_{P_3}^*(\zeta)}{|T_{P_1}(\zeta)|^2 + |T_{P_2}(\zeta)|^2 + |T_{P_3}(\zeta)|^2 + \alpha} \right] \quad (11)$$

where α is regularization parameter according to the noise level of intensity images. It should be noted that although the idea of MFC method has been previously proposed in 2D phase imaging based on multiple propagation distances [42, 43], here we first extend this approach to the 3D tomographic imaging and combine different illumination apertures to obtain improved result of 3D RI reconstruction.

It should be also noted that in order to achieve a more complete and balanced frequency coverage, the shapes and coherent parameters of the three illumination apertures have to be chosen properly. For normal circular apertures, smaller coherence parameter provides stronger intensity contrast but can only cover the low-frequency regions. Increasing the coherence parameter results in larger frequency support at the expense of reduced intensity contrast. A wide-open circular aperture is not suitable for RI reconstruction because the intensity contrast gradually vanishes when the coherence parameter approaches 1. This issue can be solved by replacing the conventional circular aperture with an annular one, which can achieve a broadband frequency coverage and enhanced response in both low- and high-frequencies. In this work, we choose to use circular aperture with coherent parameter 0.32 to fill in the low frequency components. Another circular aperture with coherent parameter 0.65 is also used because it provides a good tradeoff between the frequency coverage (especially medium frequencies) and intensity contrast, which is previously used in (single-aperture) PC-ODT [35, 38]. Finally, an annular aperture with coherent parameter 0.95 is used to make use of the full NA range of illumination optics and extent the lateral frequency response to 2NA of objective.

To provide a more intuitive explanation of used aperture setting, we compare the final 2D sections of combined 3D POTF with the nonzero region of entire volume transmitted through the incoherent system, as shown in Fig. 6. Three lateral spatial frequency positions, which correspond to low, medium and high frequencies, are selected for comparison, and the line profiles at these frequency locations along axial direction are plotted in the $u-w$ plane in Fig. 6(c). Moreover, the line profiles at the same positions in the ideal low-pass filter of incoherent system are plotted as well. From the profiles of POTFs, the responses of selected frequency positions are non-zero and provide relatively high SNR in the pass-band of ideal 3D POTF. The high-frequency component, especially the region enclosed by the yellow lines [see Fig. 6(a)] are mainly contributed by the annular illumination aperture, which is also reflected in the profiles f_{a1} and f_{a3} in Fig. 6(c). It should be noted that, due to the complicated form of 3D POTF, solving for optimum source pattern combination is quite challenging. The current choice was empirically designed based on intuitive criteria related to the shape and response of the synthesized POTF. It provides a good tradeoff between the frequency coverage and the aperture number. There is no doubt that if we use more than 3 illumination apertures, the final RI reconstruction can even be more robust and accurate. However, the image acquisition process will become more time-consuming, and the tradeoff between resolution and contrast cannot be overcome without using the annular aperture.

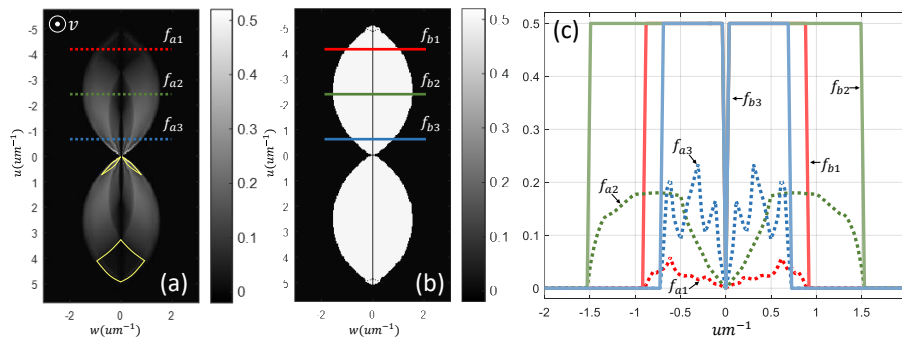


Fig. 6. 2D section comparison results between 3D POTF after MFC and ideal low-pass POTF. (a) Combined POTF using multiple illumination aperture. Three lateral spatial frequency positions are selected for comparison, and the frequency components mainly contributed by annular illumination aperture are marked with yellow line. (b) Ideal low-pass POTF determined by the nonzero region of entire volume transmitted through the incoherent system. (c) The profiles of combined POTF and ideal low-pass one.

3. Implementation of MFC-ODT technique

The proposed MFC-ODT technique is implemented based on an inverted commercial microscope (IX83, Olympus) equipped with an oil-immersion objective lens (Olympus UPLSAPO 100 \times , NA = 1.4) and an oil-immersion condenser type top lens (Olympus, NA = 1.4, $n_{oil} = 1.515$, maximum incident angle = 67.5 $^\circ$), as depicted in Fig. 7. A halogen white light source with a green interference filter is used for illumination, which can provide quasi-monochromatic lights with narrow bandwidth (central wavelength $\lambda_0 = 550$ nm, ~ 10 nm bandwidth). The image is captured with a scientific CMOS (sCMOS) camera (Hamamatsu, Orca Flash 4.0 V3, 6.5 μm pixel pitch). The annular aperture used in this work is custom-built by a thin circular glass plate with the opaque regions, and the radius of central opaque circular region, anodized and dyed with a flat-black pigment, is 0.95 (normalized). This annular plate is fitted into an open slot positions in the condenser turret and properly centered in the optical pathway. The axial scanning of intensity stack is realized by a motorized focus drive with a step size of 0.1 μm . In our case, three sets

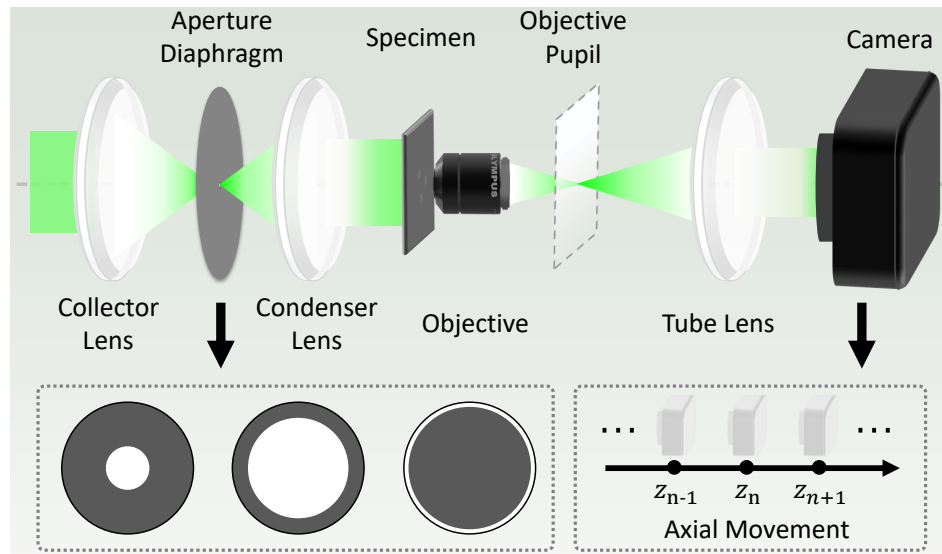


Fig. 7. Schematic diagram of experimental setup. The illumination aperture before the condenser lens can be replaced by the circular and annular shaped aperture in the condenser turret and three intensity stacks are captured under respective illumination pattern.

of data are measured under different illumination apertures and each intensity stack contains 100 images with 400×400 pixels. The coherence parameters of two respective circular-shaped apertures are 0.32 and 0.65, respectively, and the normalized ring width of annular aperture is 0.05, as shown in Fig. 7. The spatial sampling rates in x , y and z directions are $0.065 \mu\text{m}$, $0.065 \mu\text{m}$ and $0.1 \mu\text{m}$, respectively.

As for the image acquisition and data processing time, the exposure times corresponding to two circular apertures and annular aperture are set to 15 ms, 10 ms and 30 ms in our experiments, respectively. All the experimental data is processed by MATLAB software (MATLAB R2016a) with a personal computer (Intel Core i7-8700K, 3.7 GHz, 16 GB DDR4 RAM), and the time required for all computation processes (including two iterations of iterative constraint) of intensity stacks field of view (FOV) ($400 \times 400 \times 100 \times 3$) is about 4.5 seconds.

4. Experimental results

First, we implement the MFC-ODT technique to a control sample for the 3D quantitative RI reconstruction. The micro polystyrene bead (Polysciences, $n = 1.59$ at $\lambda_0 = 589 \text{ nm}$) with $6 \mu\text{m}$ diameter is immersed in RI matching oil (Cargille, $n_m = 1.58$). Figure 8 displays the comparative results of three types of apertures, and the final reconstruction results of micro sphere using MFC-ODT method. In Figs. 8(a)-8(c), we show the axial raw intensity and Fourier spectrum slices for circular illumination aperture with 0.9 NA ($\rho_s = 0.65$), 1.33 NA ($\rho_s = 0.95$) and annular aperture with 1.4 NA (ρ_s of outer ring equals 1). The average values of three sets of intensity slices are normalized to 1, and the display dynamic range of intensity spectrum is fixed and set from -1 to 17. It can be seen that the image contrast of Figs. 8(a1) and 8(c1) is much higher than that of Fig. 8(b1), which is consistent with the simulation results illustrated in Fig. 3. Besides, the transmitted frequencies in the Fourier spectrum of each intensity stack match well with the corresponding POTF in shape, as shown in Figs. 8(a2), (b2), and (c2).

Figures 8(d)-8(f) are the recovered lateral and axial RI slices using the direct deconvolution method (with only single aperture), and the regularization parameter α is set to 10^{-3} for MFC

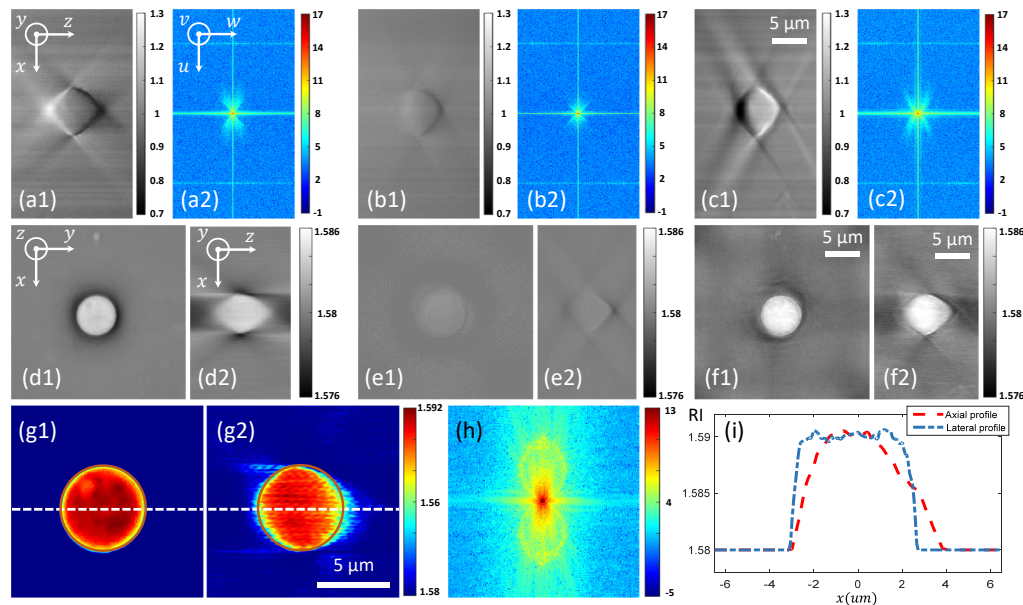


Fig. 8. RI experimental results of micro polystyrene bead with $6 \mu\text{m}$ diameter. (a-c) Raw images of captured intensity stacks and Fourier spectrum sections under three different illumination apertures. (d-f) Recovered lateral and axial slices using the direct deconvolution equation. Especially, figure (e) is added with the appropriate contrast for the display propose. (g) Final 3D RI slices with same pixel sampling in all directions. (h) Final recovery of Fourier spectrum after iterative constraint. (i) Axial and lateral RI profiles of reconstructed micro bead. Scale bar, $5 \mu\text{m}$.

method and 5×10^{-5} for Fig. 8(e), respectively. Although the recovered axial resolution of RI slice under wide-open circular aperture shown in Fig. 8(e2) is better than the result shown in Fig. 8(d2), the RI contrast in Fig. 8(e) is too weak compared with RI results in Figs. 8(d) and 8(f). Furthermore, in order to achieve more accurate 3D RI reconstructions, the iterative reconstruction algorithms with non-negative and total variation regularization [44, 45] are applied to the final RI stack. The pixels whose RI values are smaller than the RI of the surrounding medium are forced to be the same as the medium RI, and the total variation regularization is implemented based on split Bregman iterations. It should be noted that in the iterative constraint algorithm, the initially reconstructed RI in the Fourier space based on MFC method is regarded as the experimentally measured data (within the support of the synthesized POTF), which is used to build the data fidelity term. The iterative constraint algorithm generally generates reasonably accurate predictions for the missing angle region that cannot be covered by the POTF. After two iterations of constraint, the negative RI bias is removed and the missing cone effect is significantly alleviated. The final RI distributions and Fourier spectrum slices of reconstructed micro bead are presented in Figs. 8(g) and 8(h) with same sampling rate of $0.065 \mu\text{m}$ in all directions. And the final reconstructed RI maps are marked with two dark red circles for the comparison of the exact profile. Figure 8(h) shows the axial section of RI Fourier spectrum of the bead. Although the concentric ring pattern is dense, it can still be distinguished in Fig. 8(h). Four semicircular arcs of Ewald sphere form the entire frequency volume transmitted through the imaging system, and the axial and lateral imaging resolutions are extended to maximum theoretical limits of an incoherent microscope. Due to the missing cone problem as well as the imbalanced coverage of the POTF in lateral and axial directions, the recovered bead still suffers from slight elongation and RI underestimation along the axial direction, as shown in Fig. 8(i). Overall, both the 3D

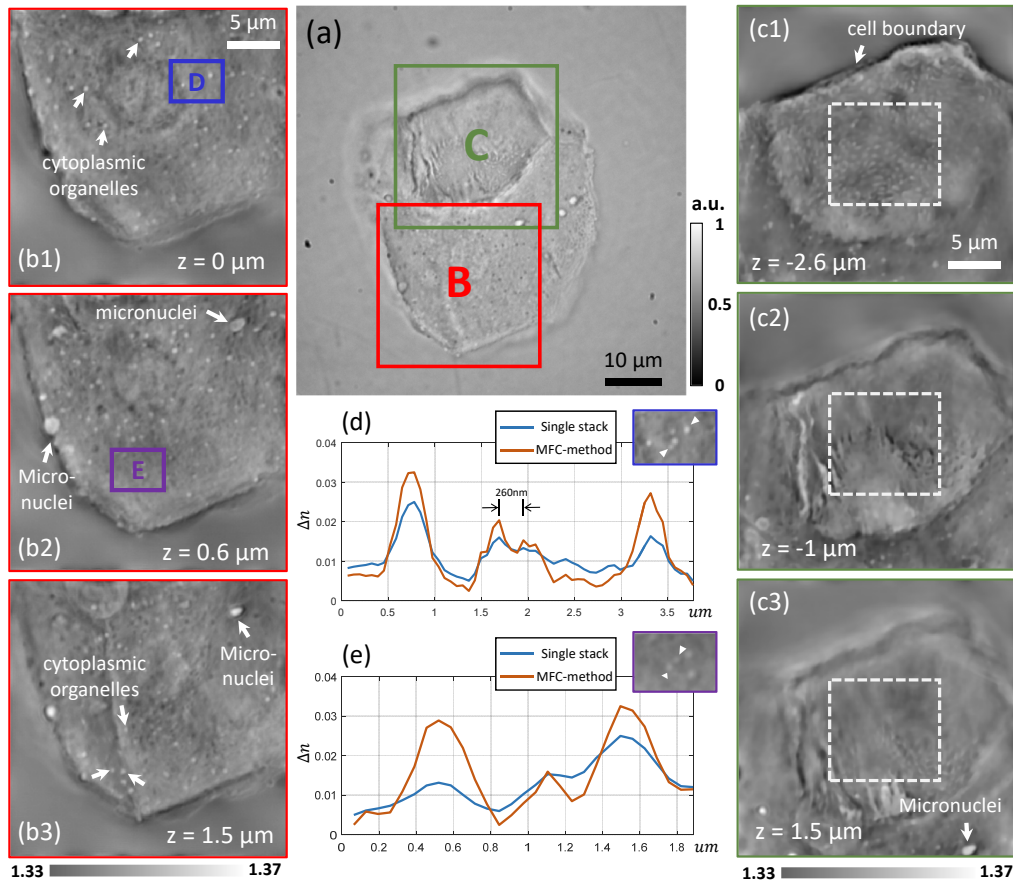


Fig. 9. Tomographic reconstruction of human buccal epithelial cell. (a) The captured raw intensity image of full sensor FOV under circular illumination aperture with $\rho_s = 0.65$. (b-c) Detailed RI slices at different axial planes of two enlarged regions, see also [Visualization 1](#). (d-e) Comparative profile lines of quantitative RI measurement between single stack and MFC method for two selected small regions. The achievable lateral resolution of MFC-ODT technique is up to 260 nm. Scale bar denotes 10 μm and 5 μm , respectively.

shape and the RI of the micro polystyrene bead are successful reconstructed, which verifies the validity and accuracy of the proposed MFC-ODT method.

In order to test the performance of MFC-ODT in its intended biomedical applications, unstained fresh human buccal epithelial cell (cheek cell) smear is used for the 3D RI measurement. The cheek cells are placed in the gap between two thin *no. 0* coverslips with 0.9% sodium chloride matching solution ($n_{\text{water}} = 1.33$). It is worth mentioning that the pupil of condenser lenses should be adjusted while the RI of the surrounding medium does not match the design medium of the lenses used. For the case where the RI value of the surrounding medium n_m is smaller than the value of illumination NA NA_{ill} , the effective illumination NA is determined by the RI of surrounding medium instead of the NA of condenser lenses. Figure 9(a) is the captured raw intensity image of full sensor FOV under circular illumination aperture with $\rho_s = 0.65$. Two representative regions, labeled B and C, are selected for the detailed analysis, and the enlarged RI reconstruction slices of these regions at three different axial positions are shown in Figs. 9(b) and 9(c), respectively. Moreover, the optically dense micronuclei and some large cytoplasmic organelles are shown with distinguishable RI contrast and high clarity in Figs.

9(b1)-9(b3). In Fig. 9(c), the region C shows the cell boundary, bacteria (diplococci mostly) on the surface of cells and the RI changing of the squamous structures in cytoplasm from the top to the bottom plane. Besides, two measured comparative RI line profiles of two sub-regions in Fig. 9(b) using multiple stacks and single stack ($\rho_s = 0.65$) are presented in Figs. 9(d)-9(e). These line plots demonstrate that by combining several illumination apertures, the MFC-ODT technique significantly improves the imaging resolution compared to conventional PC-ODT method. The smallest cytoplasmic organelle structures have a separation of only 260 nm, which can only be resolved by the MFC-ODT technique. The final recovered RI stacks along axial direction for two different regions are also provided in [Visualization 1](#) as a through-slice video for better visualization.

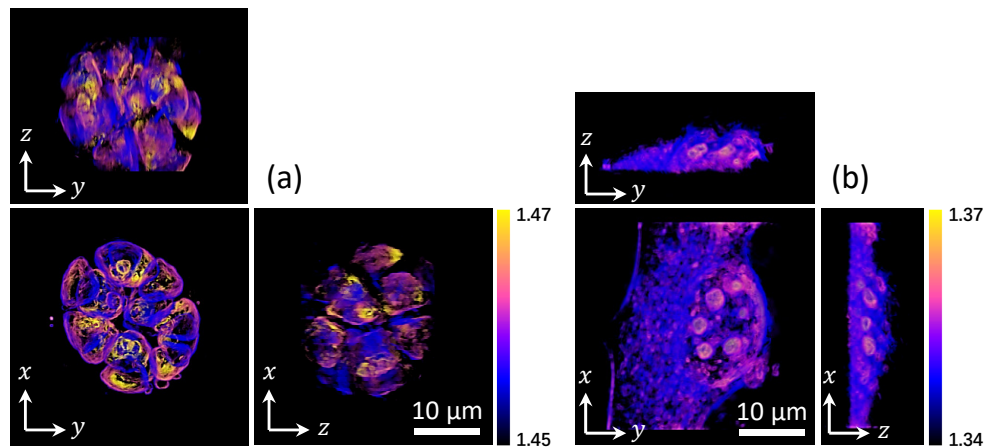


Fig. 10. 3D RI tomograms rendering of (a) *Pandorina morum* algae and (b) HeLa cell in $x - y$, $z - y$ and $x - z$ planes. Scale bar, 10 μm .

Finally, the proposed MFC-ODT technique is applied to a bleached paraffin section of *Pandorina morum* algae (*P. morum*) and a HeLa cell immersed in culture medium. Figure 10 shows the 3D rendering results of *P. morum* and HeLa cell in $x - y$, $z - y$ and $x - z$ directions, respectively. Besides, the recovered through-slice RI stacks of these two samples as well as the corresponding 3D rendered images are animated in [Visualization 2](#) and [Visualization 3](#), respectively. *P. morum* is a genus of green algae composed of 8, 16, or sometimes 32 cells, and these cells are held together at their bases to form a sack globular colony surrounded by mucilage. The cells of *P. morum* form an ellipsoid spheroid with a distinct anterior-posterior polarity, so this *P. morum* is an ideal thick object suitable for 3D tomographic imaging. In our experiment, the sample is cleaned with H_2O_2 and immersed in the fixed embedding medium (paraffin wax, $n_{wax} = 1.45$). In the 3D rendered tomogram of *P. morum* [Figure 10(a) and [Visualization 2](#)], the 16 individual cells are clearly visualized, and we can see clearly how different cells of the algae stack with respect to each other in 3D space. The HeLa cell is immersed in culture medium, and the RI of culture medium $n_m = 1.34$. Although the 2D quantitative phase information can provide quantitative characterization of the HeLa cell, the 3D RI distribution provides more detailed sub-cellular features in different axial planes instead of an integral along the axial direction. The results shown in Fig. 10(b) and [Visualization 2](#) reveal that we can clearly image the details of the 3D structures of a single cell throughout its entire volume as well as quantify the RI of subcellular organelles. The nucleoli inside the cell have higher RI value compared to the average index of cytoplasm, and the rendered 3D RI image provides much clearer information about the actual structure of the HeLa cell.

5. Conclusion and discussion

In summary, we demonstrate a novel tomographic technique termed MFC-ODT by combining different frequency components corresponding to different illumination apertures in a traditional bright-field transmission microscope with partially coherent illuminations. The expression of 3D POTF for an arbitrary illumination source is re-derived, and the effect of 3D POTF on the resolution and SNR of RI reconstruction is analyzed, especially for the case of annular illumination aperture. In order to obtain a more complete frequency coverage and balanced transfer function, we choose to use two circular apertures with coherent parameters of 0.32 and 0.65 and one annular aperture with coherent parameter of 0.95. The corresponding three 3D POTFs are synthesized based on a linear least-squares method, resulting in high-quality 3D RI reconstruction with improved resolution and SNR. It is shown that the MFC-ODT can achieve a resolution up to twice the coherent diffraction limit theoretically, and provide robust reconstruction for both low and high frequencies within the Ewald sphere. The validity and effectiveness of the proposed MFC-ODT technique are demonstrated by 3D RI reconstruction and rendering of micro bead and various biological specimens.

It should be noted that the current choice of aperture setting was empirically designed based on intuitive criteria related to the shape and response of the synthesized POTF. Theoretically, such a heuristic approach cannot guarantee optimality for the solution; nevertheless, in practice the proposed aperture setting can give satisfactory performance. If a programmable aperture is used, the illumination aperture should not just be limited to circular or annular shapes but can be an arbitrary 2D function. Enabling the use of a more elaborate criterion (merit function) based on the response and frequency coverage of the POTF for evaluating the “goodness” of an aperture, and optimizing the aperture function and combination based on some optimization algorithms are interesting directions for future work. Besides, the main theory of MFC-ODT is heavily based on the previous PC-ODT technique, which is only valid under first order Born approximation. However, as is widely recognized that the first order Rytov approximation enables more accurate imaging of thick biological samples [18]. Therefore, extending the scope of application of PC-ODT to Rytov approximation is another important direction that requires further investigation.

Funding

National Natural Science Fund of China (61722506, 61505081, 111574152); Final Assembly ‘13th Five-Year Plan’ Advanced Research Project of China (30102070102); Equipment Advanced Research Fund of China (61404150202); National Defense Science and Technology Foundation of China (0106173); Outstanding Youth Foundation of Jiangsu Province of China (BK20170034); The Key Research and Development Program of Jiangsu Province, China (BE2017162); ‘Six Talent Peaks’ project of Jiangsu Province, China (2015-DZXX-009); ‘333 Engineering’ Research Project of Jiangsu Province, China (BRA2016407); Fundamental Research Funds for the Central Universities (30917011204, 30916011322).

Disclosures

The authors declare that there are no conflicts of interest related to this article.